The Madden–Julian Oscillation Recorded in Early Observations from the Tropical Rainfall Measuring Mission (TRMM)

Hirohiko Masunaga, Tristan S. L'Ecuyer, and Christian D. Kummerow

Colorado State University, Fort Collins, Colorado

ABSTRACT

A satellite data analysis is performed to explore the Madden–Julian oscillation (MJO) focusing on the potential roles of the equatorial Rossby (ER) and Kelvin waves. Measurements from the Tropical Rainfall Measuring Mission (TRMM) Precipitation Radar (PR) and Visible/Infrared Scanner (VIRS) are analyzed in the frequency–wavenumber domain to identify and ultimately filter primary low-frequency modes in the Tropics. The space–time spectrum of deep-storm fraction estimated by PR and VIRS exhibits notable Kelvin wave signals at wavenumbers 5–8, a distinct MJO peak at wavenumbers 1–7 and periods of about 40 days, and a signal corresponding to the ER wave. These modes are separately filtered to study the individual modes and possible relationship among them in the time–longitude space. In 10 cases analyzed here, an MJO event is often collocated with a group of consecutive Kelvin waves as well as an intruding ER wave accompanied with the occasional onset of a stationary convective phase. The spatial and temporal relationship between the MJO and Kelvin wave is clearly visible in a lag composite diagram, while the ubiquity of the ER wave leads to a less pronounced relation between the MJO and ER wave. A case study based on the Geostationary Meteorological Satellite (GMS) imagery together with associated dynamic field captures the substructure of the planetary-scale waves. A cross-correlation analysis confirms the MJO-related cycle that involves surface and atmospheric parameters such as sea surface temperature, water vapor, low clouds, shallow convection, and near-surface wind as proposed in past studies. The findings suggest the possibility that a sequence of convective events coupled with the linear waves may play a critical role in MJO propagation. An intraseasonal radiative–hydrological cycle inherent in the local thermodynamic conditions could be also a potential factor responsible for the MJO by loosely modulating the envelope of the entire propagation system.

1. Introduction

Since first documented by Madden and Julian (1971, 1972), the Madden–Julian oscillation (MJO) has been extensively studied to explore its physical mechanism. In contrast to other low-frequency modes such as the Kelvin wave, however, the MJO has no apparent counterpart in the linear shallow-water theory described by Matsuno (1966). Numerous attempts have been made to explain the physical processes that give rise to the MJO. In the framework of the linear theory, the equatorial Kelvin wave best shares fundamental characteristics with the MJO in reference to the fact that both propagate only eastward and are restricted to the Trop-

ics. On the other hand, the typical period of the MJO is substantially longer than expected from the Kelvin wave speed. A variety of theories proposed to date (see review by Hayashi and Golder 1993) are in agreement on the critical importance of the moist processes. The MJO has been extensively studied with emphasis on the role of convection by both observational data analyses (e.g., Nakazawa 1988; Takayabu and Murakami 1991; Hendon and Salby 1994; Yanai et al. 2000) and model studies (Hayashi and Sumi 1986; Lau et al. 1989; Bladé and Hartmann 1993; Grabowski 2003; among others).

Consensus, however, has yet to be achieved in the comprehensive understanding of the MJO. Slingo et al. (1996) conducted a comparison study using 15 atmospheric general circulation models (AGCMs) to test their ability to predict the MJO. They found that AGCMs could typically produce eastward propagation similar to the MJO, but most of them failed to simulate periods longer than 30 days. A frequency–wavenumber

Corresponding author address: Dr. Hirohiko Masunaga, Dept. of Atmospheric Science, Colorado State University, Fort Collins, CO 80523.
E-mail: masunaga@atmos.colostate.edu

analysis of a long-term (~18 yr) record of outgoing longwave radiation (OLR) found that the spectral peak corresponding to the MJO clearly does not belong to the Kelvin wave solution with any equivalent depth (Wheeler and Kiladis 1999, hereafter WK99). A number of papers discussed the MJO in the context of interactions between different types of tropical oscillations (Dunkerton and Crum 1995; Wheeler and Weickmann 2001; Straub and Kiladis 2003; Roundy and Frank 2004b,c). Some observational studies revealed the intraseasonal cycle of local imbalance in the radiation and moisture budget associated with convective variability (Zhang 1996; Flatau et al. 1997; Stephens et al. 2004).

The present work investigates the MJO as well as other low-frequency tropical waves using precipitation measurements by satellite remote sensing. The analysis is based on measurements from the Tropical Rainfall Measuring Mission (TRMM) satellite, National Oceanic and Atmospheric Administration (NOAA) satellite, and Geostationary Meteorological Satellite (GMS) data. Section 2 describes the data employed in this work. A frequency–wavenumber analysis is performed in section 3 to sort out the MJO and convectively coupled equatorial waves in the spectral domain. Applying bandpass filters in order to separate different wave modes, the individual modes as well as the potential interrelationship of planetary-scale waves is investigated in the time–longitude space (section 4). Section 5 is devoted to discussion on the result. The findings are summarized in section 6.

2. Data

A major part of the analysis is based on a combination of data from the Precipitation Radar (PR) and Visible/Infrared Scanner (VIRS) onboard the TRMM satellite. The TRMM orbit is sun-asynchronous and has the recurrence cycle of about 23 days in local solar time. This cycle would be twice as long if the ascending and descending paths are discriminated from each other. Among the TRMM operational data archives, the PR echo-top height or storm height is provided by the TRMM 2A23 product, and the VIRS channel-4 (10.8 μm) radiance (hereafter IR T_b, after conversion to brightness temperature) is given by the 1B01 dataset. VIRS pixels are collocated with PR over the inner portion of the VIRS swath that overlaps the narrower PR swath. Nonoverlapping VIRS pixels are not used in the analysis to avoid sampling inconsistency with the PR.

In this paper, the deep-storm fraction is used as a measure of the intensity of active convection. The deep-storm fraction is the area fraction of precipitation events having VIRS IR T_b colder than 245 K and PR echo-top height higher than 4 km. This definition is the combination of deep stratiform and deep convective systems in terms of the storm categorization defined by Masunaga et al. (2005). Although infrared radiance by itself is a reasonable proxy of deep convection, it is sensitive to all high clouds including detrained cirrus clouds, which predominate precipitation cores in spatial and temporal extent. On the other hand, the deep-storm fraction is more directly linked with the moist processes. The simultaneous use of the VIRS and PR excludes both nonprecipitating high clouds and rainfall with relatively warm cloud tops (i.e., cumulus congestus) from the analysis. The deep-storm fraction is calculated over each 2.5° × 1-day box in the time–longitude space with the latitudinal coverage of 10°S–10°N. The meridional band is divided by the equator for the symmetric/antisymmetric decomposition in frequency–wavenumber analysis. It is noted that the daily dataset is longitudinally continuous when integrated over 10°S–0° and 0°–10°N, although each 2.5° × 10° box is only partially sampled, where the subgrid area coverage is ~23% on average. Because no grid box of this size is left empty on any given day, spatial interpolation is not required on a daily basis except for some irregular cases mentioned below.

Two time periods are analyzed: 21 December 1997 to 10 December 1999 (720 days) and 3 December 2000 to 20 June 2001 (200 days). The primary distinction between these periods is that the first encompasses a portion of the 1997–98 El Niño and the subsequent La Niña phase, while the second represents a normal phase of the El Niño–Southern Oscillation (ENSO). MJO activity is moderate throughout the both periods except for the first few months of the second period, which exhibits a relatively strong peak in terms of the real-time multivariate MJO index computed by Wheeler and Hendon (2004). This ensures that the analysis conducted here represents average MJO events without skewing the focus toward extreme cases. The first period contains 16 days of data that are partially missing and nine other days entirely devoid, primarily due to sensor shutoffs. There are, however, no consecutive periods of missing data in excess of four days, so the missing data can be filled in by linear interpolation in time with no visible impact on the analysis of low-frequency oscillations. There are no data missing during the second period.

To assess the magnitude of potential sampling errors inherent in deep-storm fraction, VIRS IR T_b values are first compared with the NOAA-interpolated OLR (hereafter NOAA OLR). The NOAA OLR dataset, constructed from NOAA's polar-orbiting satellite data, has been interpolated spatially and temporally to a

daily, $2.5° \times 2.5°$ grid. The satellite in use for the time periods mentioned above is NOAA 14 (NOAA 16) before (on and after) 1 March 2001. NOAA OLR was derived from window-channel radiance through an analytic formula (Gruber and Krueger 1984). Since the flux equivalent blackbody temperature is almost linearly related to the equivalent blackbody window temperature in their formula, OLR and IR T_b are essentially equivalent in the relative strength of spectral power. These data are used to ensure that spectral features of interest are statistically meaningful by identifying satellite-dependent spurious peaks in VIRS IR T_b spectra relative to those derived using NOAA OLR. The deep-storm fraction is then examined once spectral artifacts specific to TRMM measurements are isolated based on VIRS IR T_b.

Geostationary satellite data are also analyzed for investigating the substructure of convectively coupled waves. *GMS-5*, operated by the Japan Meteorological Agency, is used for a region covering the Maritime Continent and the west and central tropical Pacific (10°S–10°N and 80°E–160°W) from 21 April to 20 May 2001. Infrared channel-1 (11 μm) brightness temperature is gridded on a half-degree scale with a temporal resolution of 3 h. The daily dataset of 850-hPa horizontal winds is adopted from the National Centers for Environmental Prediction–National Center for Atmospheric Research (NCEP–NCAR) reanalysis data.

3. Frequency–wavenumber analysis

Frequency–wavenumber analysis of satellite measurements has been a popular tool to explore convectively coupled tropical waves in terms of visible brightness (Gruber 1974; Zangvil 1975), infrared flux (Nakazawa 1986; Salby and Hendon 1994; Takayabu 1994; WK99; Roundy and Frank 2004a), or direct precipitation measurements (Cho et al. 2004; Benedict and Randall 2006, manuscript submitted to *J. Atmos. Sci.*). In this study, infrared brightness temperature and the deep-storm fraction are examined in the space–time spectral domain utilizing the entire period of 920 (720 + 200) days described in section 2. The method of analysis is first described in section 3a, followed by the results in section 3b.

a. Analysis scheme

Our method of frequency–wavenumber analysis is similar to the scheme developed by WK99. The only major difference from WK99 lies in the definition of the reference noise spectrum used to test statistical significance. While WK99 defined the background spectrum by smoothing spectral peaks out, the red noise spectrum is employed here as described later. The red noise spectrum is adopted for the sake of minimizing the arbitrariness in defining the background spectrum. A background spectrum constructed from multiple passes of smoothing filters solely relies on the number of the filters applied, which is a rather subjective choice of the user. The red noise spectrum, on the other hand, provides a more objective basis against which the statistical significance of spectral peaks is tested. Note that a 1–2–1 filter is modestly used in this study to remove stochastic fluctuation in the red noise spectrum, but it only plays a minor role in determining the overall structure of the noise spectrum.

The time–longitude sections of the deep-storm fraction, TRMM IR T_b, and NOAA OLR are converted into the wavenumber–frequency domain in the following manner. First, each variable is decomposed into symmetric and antisymmetric components about the equator as $[f(\text{NH}) + f(\text{SH})]/2$ and $[f(\text{NH}) - f(\text{SH})]/2$, respectively, where $f(\text{NH})$ and $f(\text{SH})$ denotes the quantity in the Northern and Southern Hemispheres, respectively, at a same longitude. This procedure helps separate different wave modes by the parity of their eigenfunctions as originally demonstrated by Yanai and Murakami (1970). Next, these datasets are divided into segments of 80 consecutive days. The beginning dates of sequential segments are selected at an interval of 40 days so that each segment overlaps by a half in length. The overlap is aimed at minimizing the loss of signals due to the data windowing (described below) and the truncation of low-frequency waves. Sinusoidal backgrounds with the periods of one, a half, and a quarter year are removed from OLR data to factor the seasonal cycle out. This step is skipped for the deep-storm fraction because the seasonal variation has no direct influence on the deep-storm fraction, whereas it periodically offsets OLR. The mean and linear components in time identified by least square fit are further subtracted at each longitude. The data are then tapered to zero at both ends of the time series using the Hanning (or cosine bell) window. This windowing technique is intended to mitigate side lobes in the spectrum cause by the discontinuity at the ends of a time sequence. Complex fast Fourier transformation (FFT) is applied in longitude and in time to each 80-day segment. The resulting space–time spectrum, having a bandwidth of 0.0125 (1/80) cycles per day (cpd) in frequency and one zonal wavenumber, is averaged over all 19 segments formed from the data in the two time periods (section 2).

The statistical significance of the obtained spectral power is evaluated in comparison with the red noise
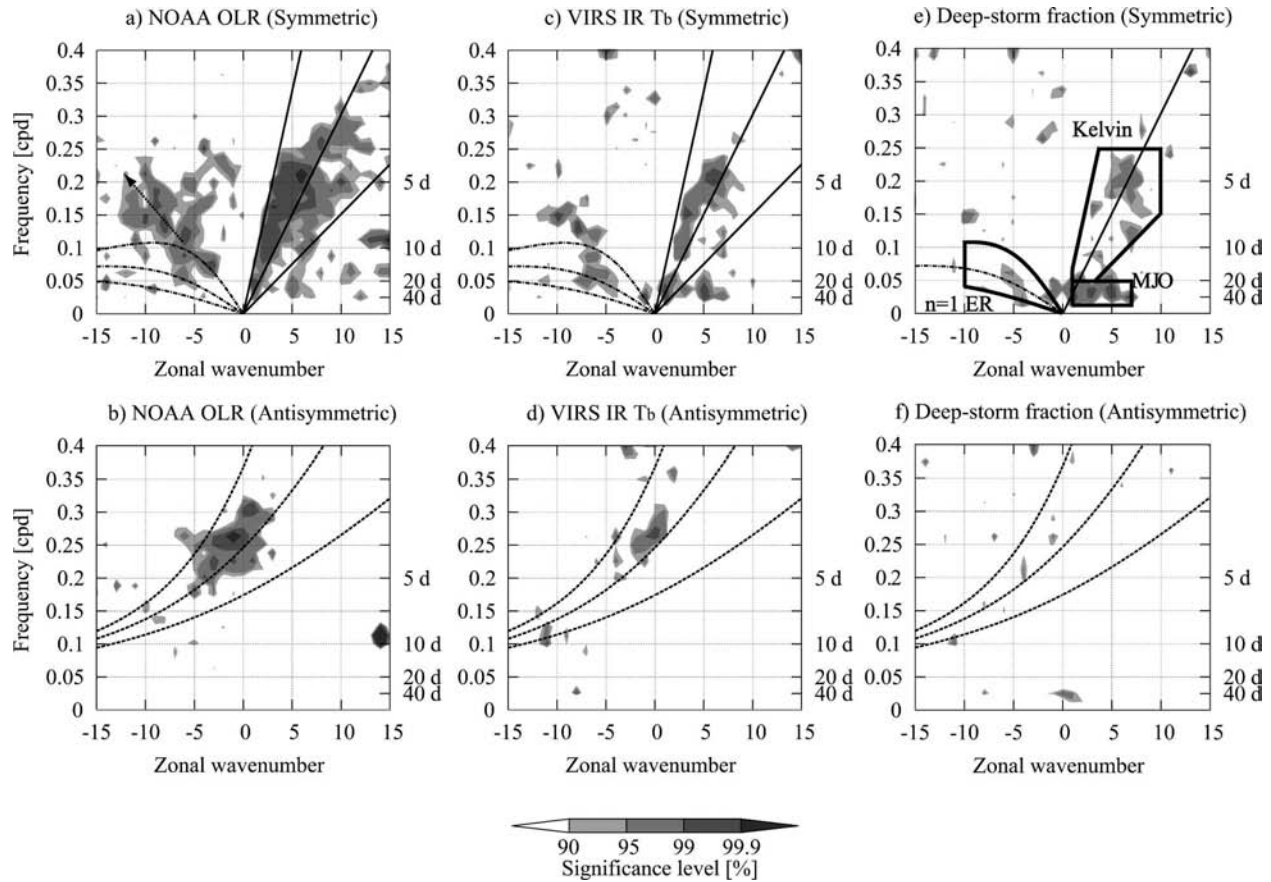
FIG. 1. The symmetric and antisymmetric spectra in the frequency–wavenumber domain of (a), (b) NOAA OLR, (c), (d) TRMM IR T_b, and (e), (f) deep-storm fraction. Positive (negative) wavenumbers correspond to eastward (westward) propagation. Superimposed are the theoretical dispersion relations of the Kelvin wave (solid straight lines), MRG and $n = 0$ EIG waves (dashed curves), and $n = 1$ ER wave (dotted–dashed curves) for the equivalent depths of 5, 20, and 100 m, from bottom to top. The arrow in (a) indicates a westward phase speed of 8 m s^{-1}. Bandpass filters are designated by thick lines in (e).

spectrum. The explicit form of the red noise spectrum p_{rn} is given as (section 11.2.5 in von Storch and Zwiers 1999)

$$p_{rn}(k, \omega) = \frac{\sigma_z^2(k)}{1 + \alpha_1(k)^2 - 2\alpha_1(k) \cos(2\pi\omega)}, \quad (1)$$

where k is zonal wavenumber, ω is frequency, σ_z^2 is the variance of driving white noise, and α_1 is lag-1 autocorrelation coefficient computed from the observed time series whose longitudinal component is transformed into wavenumber space. The amplitude of the red noise spectrum σ_z^2 is determined so that Eq. (1) is equivalent to the mean of the symmetric and antisymmetric components of the actual spectra when integrated over frequency. Once α_1 and σ_z^2 are determined for each wavenumber, the stochastic fluctuation across k in $\alpha_1(k)$ and $\sigma_z^2(k)$ is removed by applying multiple passes of a 1–2–1 filter. Statistical significance is then tested against the

red noise spectrum to purify spectral peaks of interest from day-to-day weather variations.

b. Results

Figures 1a–d show the symmetric and antisymmetric components of NOAA OLR and TRMM IR T_b in the frequency–wavenumber domain. Eastward (westward) propagation is designated by positive (negative) zonal wavenumbers. The dispersion relations for some dominant low-frequency modes of tropical waves are also depicted. These theoretical curves are based on the shallow-water solutions derived by Matsuno (1966), allowing a wide range of equivalent depths h that account for various vertical modes with different wavelengths (Lindzen 1967). The thermodynamic environment that controls the moist wave characteristics is closely linked with the processes selecting dominant modes with particular equivalent depths. A convectively coupled wave

is known to have a smaller equivalent depth, or a smaller phase speed, than its dry counterpart (WK99, and references therein). Emanuel et al. (1994), for example, provided a theoretical basis of the internal wave propagating in a convecting atmosphere, which is found to be slower than the corresponding dry mode. The Kelvin wave (shown as solid, straight lines in Fig. 1) and the $n = 1$ equatorial Rossby (ER) wave (dotted–dashed) have symmetric eigenfunctions about the equator in pressure and zonal wind. By contrast, they are antisymmetric for the mixed Rossby–gravity (MRG) wave (dashed for $k < 0$) and $n = 0$ eastward inertio–gravity (EIG) wave (dashed for $k > 0$). Three reference values of $h = 5$ m, 20 m, and 100 m, from bottom to top in Fig. 1, are chosen for the theoretical curves. These three equivalent depths correspond to 7, 14, and 31 m s^{-1}, respectively, in the Kelvin wave speed.

A prominent feature in the symmetric components of NOAA OLR is the Kelvin wave confined between $h = 20$ m and 100 m, tailed by a weaker component extended down to $h = 5$ m. The westward-propagation domain of Fig. 1a includes another striking signal, loosely centered around $v = -8$ m s^{-1} as indicated by an arrow. This signal, without any counterpart of linear wave modes, might reflect disturbances moving together with the background easterly wind. The speed of 8 m s^{-1} is close to a peak value in climatological zonal wind in the tropical upper troposphere (Wheeler et al. 2000). The easterly wave as documented by Reed and Recker (1971) also has a phase speed (9 m s^{-1}) close to this spectral mode. The antisymmetric component (Fig. 1b) shows a spectral peak associated with the MRG and $n = 0$ EIG waves.

The fact that the satellite-observed area does not completely cover the globe within a single day creates a spectral artifact in daily datasets. An observed signal blinks regularly at a constant longitudinal interval as it repeatedly appears from and hides behind satellite blind spots. The temporal and spatial periodicity of this effect generates a well-pronounced, spurious peak in spectral space. For the polar-orbiting NOAA satellites, an artificial peak appears at $k = 14$ and $\omega = 0.11$ cpd as seen in Figs. 1a,b, corresponding to the number of swaths swept per day ($=14$) and the 9-day repeat cycle of satellite zenith overpass.

Spectral power turns out to be generally weaker for VIRS IR T_b (Figs. 1c,d) than for NOAA OLR. This can be ascribed to sampling errors specific to the orbital configuration of the TRMM sensors. Complete observational coverage at tropical latitudes takes about 7 days for the PR swath width of 215 km. (As mentioned in section 2, the outer portion of the VIRS swath not overlapping with the PR swath is precluded from analy-sis.) A poorer sampling makes the spectrum noisier and hence reduces the statistical significance of spectral power particularly for high-frequency modes. The Kelvin wave nonetheless exhibits a stable signal in the VIRS IR spectrum although it is narrowed to mostly above $h = 20$ m. The ER wave is readily identifiable at wavenumbers from -4 to -8, barely separable from the faster disturbances outside the ER wave domain. The antisymmetric spectrum has a confined signal of the MRG/$n = 0$ EIG wave around $k = 0$. The TRMM spectrum also has a spectral artifact due to finite orbital coverage, except that it falls outside the range of Fig. 1 around $k = 15$–16 and $\omega = 0.4$–0.45 cpd.

The sun-asynchronous TRMM orbit could yield a resonance effect between the diurnal cycle of convective activity and the TRMM orbital precession: an oscillation with a period close to 23 days can be selectively amplified. Cho et al. (2004) examined potential sampling errors in a space–time spectrum of TRMM measurements and found no serious contamination by the diurnal cycle for equatorial wave modes. Indeed, Figs. 1c,d shows no apparent spectral peak near 1/23 cpd in comparison with Figs. 1a,b.

Finally, frequency–wavenumber analysis is applied to the deep-storm fraction defined in section 2. Figures 1e,f shows the symmetric and antisymmetric spectra of the deep-storm fraction. Overall, statistically significant signals are even more limited than in the VIRS IR spectrum. Cho et al. (2004) also found that spectral peaks are less distinct for precipitation than for OLR except at very low frequencies. NOAA OLR and VIRS T_b indeed lack statistically significant peaks at very low frequencies (periods longer than 40 days), while the deep-storm fraction has a strong spectral signal extending down to a period of 80 days. The Kelvin wave is now shrunk into an island of high-wavenumber modes around $k = 5$–8 and $\omega = 0.15$–0.25 cpd as well as several isolated spikes. Note that a separate component at $k = 1$–2 in the Kelvin wave domain is categorized into the MJO as described below. The deep-storm fraction lacks the Kelvin modes at wavenumbers 3 and 4, for which infrared spectra exhibit pronounced evidence. This contrast may suggest that infrared radiance is not necessarily an ideal representative of the convectively coupled Kelvin wave for $k = 3$–4. These wavenumbers have relatively high equivalent depths of 20–100 m that are more likely accounted for by dry waves. Remnant anvil clouds responding to the dry Kelvin wave, therefore, likely make considerable contribution to the Kelvin wave modes with $k = 3$–4 in infrared spectra. This is also consistent with the fact that observed cloud systems documented in previous studies have a wavenumber scale of about 6–15 and propagate at a slower

speed than inferred by the infrared spectrum of the Kelvin wave (WK99). In the spectrum of the deep-storm fraction, the equivalent depth spread across both sides of 20 m at wavenumbers larger than 5.

A most remarkable feature is a slow eastward mode at periods around 40 days that extends from wavenumber 1 to 7, leading itself to a domain prohibited for the Kelvin wave. This feature is recognized as the spectral representation of the MJO, as originally indicated by WK99. Wheeler and Hendon (2004) confirmed that this spectral peak is obtained when the MJO is singled out by an EOF analysis based on a long-term record of zonal wind and OLR. Note that the apparent strength of spectral peaks can vary with different definitions of the reference noise spectrum. The red noise spectrum defined here, for example, tends to have spectral power more concentrated around low frequencies in comparison with the background spectrum as derived by WK99. This explains why the MJO peak in Fig. 1a is weaker than obtained by WK99.

Westward propagation is fainter in spectral power than the eastward modes. The ER wave is, however, noticeable around $k = -5$. The contrast in spectral strength between the Kelvin and ER waves occurs in part because the latitudinal range chosen in the analysis favors the Kelvin wave. The amplitude of the Kelvin wave is concentrated near the equator, while the ER wave has the maximum amplitude off the equator. Extending the meridional range to 15°S–15°N (not shown) actually results in a slightly stronger ER peak and a little weaker Kelvin signal in the frequency–wavenumber domain than seen in Fig. 1. General conclusions drawn from the present analysis, however, do not depend on the choice of meridional range.

In summary, the planetary-scale eastward propagation coupled with deep convection has a pair of distinct constituents: high-wavenumber ($k = 5$–8) harmonics of the Kelvin wave and the MJO mode with periods of about 40 days. The ER wave at a wavenumber of about −5 is also present but not as intense as the other two modes.

4. Time–longitude analysis

Given this identification of the dominant wave modes in the TRMM dataset, this section further examines the Kelvin wave, MJO, and ER wave in the time–longitude space and seeks to explore possible relationships between them. The filtering technique used for the time–longitude analysis is introduced in section 4a, and results are presented in section 4b. The internal structure of the planetary-scale waves are studied for a single case in section 4c to support the findings based on two-dimensional cloud images and associated dynamic field.

a. Filtering technique

The MJO, Kelvin wave, and ER wave are investigated in the time–longitude diagram by applying bandpass filters defined in the wavenumber–frequency domain. The basic method parallels that introduced by WK99, which has been widely used to date (e.g., Wheeler et al. 2000; Wheeler and Weickmann 2001; Straub and Kiladis 2003; Roundy and Frank 2004a). Each of the undivided 720-day and 200-day time series of the deep-storm fraction averaged over 10°S–10°N is decomposed into the frequency–wavenumber space after the windowing is performed in time. Data near both ends of the time series are lost due to the windowing and hence are not used in the analysis. Spectral signals bound in a given filter, with all the others eliminated, are transformed back in the time–longitude domain by backward FFT. The frequency bandwidth (1/720 or 1/200 cpd) is sufficiently small to recover all the filtered waves without the truncation of low-frequency modes.

Filters in use are designated by thick lines in Fig. 1e. The Kelvin wave filter is bounded by $1 \leq k \leq 10$, 0.05 cpd $\leq \omega \leq 0.25$ cpd (4–20 days in period), and a pair of theoretical dispersion relations with the equivalent depths of 5 m and 100 m. Periods shorter than 4 days are not used to avoid sampling noise in TRMM measurements. The MJO filter is defined as $1 \leq k \leq 7$, 0.0125 cpd $\leq \omega \leq 0.05$ cpd (20–80 days in a period), targeted on the low-frequency oscillation distinct from the Kelvin wave. The range of 20–80 days covers a majority of the observed MJO periods documented in the literature (Madden and Julian 1994). It is noted that the theoretical solution of the Kelvin wave at low wavenumbers falls within the MJO filter particularly for small equivalent depths. The $n = 1$ ER wave filter is defined between $-10 \leq k < 0$ and two dispersion relations with the equivalent depths of 5 m and 100 m.

b. Planetary-scale waves

Six 50-day time series are chosen to demonstrate the filtered MJO and Kelvin wave (in red and blue) as well as the unfiltered field (contoured) of the deep-storm fraction (Figs. 2a,b). The unfiltered field has been smoothed by running mean over 3 days in time and 15° in longitude to eliminate small-scale fluctuations. Note that this smoothing technique is not applied to the filtered waves. The subsequent analysis focuses on the 10 MJO events marked in Fig. 2, identified based on positive phases of the filtered MJO. The first three events occurred at the end of the 1997–98 El Niño, playing an

important role in the termination of the El Niño as discussed by Takayabu et al. (1999). The next three MJO events fall during the subsequent La Niña event. The remaining events are selected from a normal ENSO phase in 2001.

With the exceptions of those that occur during the El Niño (MJO-1–3), all the MJO events but MJO-8 are centered around 120°E over the Maritime Continent (Fig. 2a) and confined between the Indian Ocean (~60°E) and the date line. The regionality of convective activity associated with the MJO has been well recognized in the literature (e.g., Hendon and Salby 1994; Yanai et al. 2000; Wheeler and Hendon 2004). The visibly dominant mode of the MJO is typically wavenumber 1, while higher wavenumbers up to 7 are as pronounced as the lowest for the MJO in the space–time spectrum (Fig. 1e). The high-wavenumber modes are exaggerated than actual in the frequency–wavenumber space since the spectral power is normalized by the red noise spectrum (section 3a). Salby and Hendon (1994) pointed out that the high-wavenumber components contribute to the highly dispersive nature of the MJO, which is responsible for its regionality.

The Kelvin wave propagates at a consistently larger speed (about 15 m s^{-1} as inferred from the average equivalent depth of ~20 m) than the MJO (Fig. 2b). The Kelvin wave is occasionally visible even in the unfiltered pattern. The most conspicuous case is the one that penetrates MJO-2 through MJO-3. Intensified convection at the end of MJO-2 anchors this MJO event in the east of 60°E, making this MJO event slower than the Kelvin wave that propagates further through a subsequent ridge of the MJO. Another dramatic case is MJO-9 and MJO-10, where three notable branches of the Kelvin wave are emanated one after another at a temporal interval of about a week. A similar trend is also seen in association with other MJO events, although the Kelvin wave is less apparent in the unfiltered field. In these cases, the embedded Kelvin wave is loosely modulated in amplitude as if a few or several neighboring Kelvin waves together constitute a single MJO event.

As expected from the relatively weak spectral peak (Fig. 1), the ER mode is not a primary constituent of convectively coupled tropical waves. The ER wave (dotted in Fig. 2c) would be barely traceable from the unfiltered deep-storm fraction without contoured guidance. The ER wave, nevertheless, occasionally includes distinct spots of the enhanced deep-storm fraction when the ER wave intersects with the Kelvin wave. Figure 2d schematically illustrates the behavior of the ER and Kelvin waves in the vicinity of individual MJO events. Interestingly, each event exhibits at least one case where an ER wave intersects a moist Kelvin wave, accompanied with the interruption of the eastward propagation of convective systems or its slight westward retrogression (MJO-6, MJO-7, and MJO-10). Intensified convective systems are sometimes left behind the outgoing waves and remain unmoved (MJO-4, MJO-5, and the eastern end of MJO-7). The resulting apparent stationary convective phases always build up (besides the El Niño period) over the Indo-Pacific warm pool. Such phases, however, eventually start propagating again when they encounter an incoming Kelvin wave. A stationary convective phase otherwise dies out as seen in MJO-2, MJO-8, and MJO-9. Intensified convection is also frequently observed at the termination of entire propagation as observed at the end of MJO-6, MJO-7, and MJO-10.

To establish the statistical significance of this apparent relationship between the MJO and Kelvin/ER waves, a lag composite analysis is performed. MJO peaks are first identified as local longitudinal maxima in the MJO-filtered deep-storm fraction. The MJO peak is defined only when it exceeds $+2\sigma$ of the filtered MJO in order to assure a high signal-to-noise ratio. Fluctuations with zonal scales smaller than 30° are excluded when defining the local maxima. Higher-wavenumber fluctuations are ignored to avoid spurious signals because any spectral components with wavenumbers greater than 10 are excluded by the filters used in this study. The Kelvin and ER wave powers, that is, the square of filtered deep-storm fraction anomaly, are then composited in reference to the MJO peak with different time lags of ±7, ±3, and 0 days. The composite diagram is constructed so that the reference point (0°) coincides with the MJO peak at lag 0. All the data considered in this study (the whole globe between 10°S and 10°N for the two time series defined in section 2) are employed for the result shown in Fig. 3.

The Kelvin wave exhibits a striking peak in the vicinity of the MJO peak particularly for small time lags (within ±3 days). The Kelvin wave power at an earlier or later time (±7 days) has a weaker peak with a broader shoulder, which extends eastward (westward) for a positive (negative) lag. The MJO, in other words, tends to be accompanied with the Kelvin wave approaching from the west prior to the peak activity, after which the MJO emanates the Kelvin wave in the east. The composite series of the ER wave only shows a small, broad hump in the east of the MJO maximum with no discernible temporal evolution. The weak correlation with the MJO reflects the relatively ubiquitous nature of the ER wave, as seen, for example, around MJO-6 in Fig. 2c. The absence of temporal variability
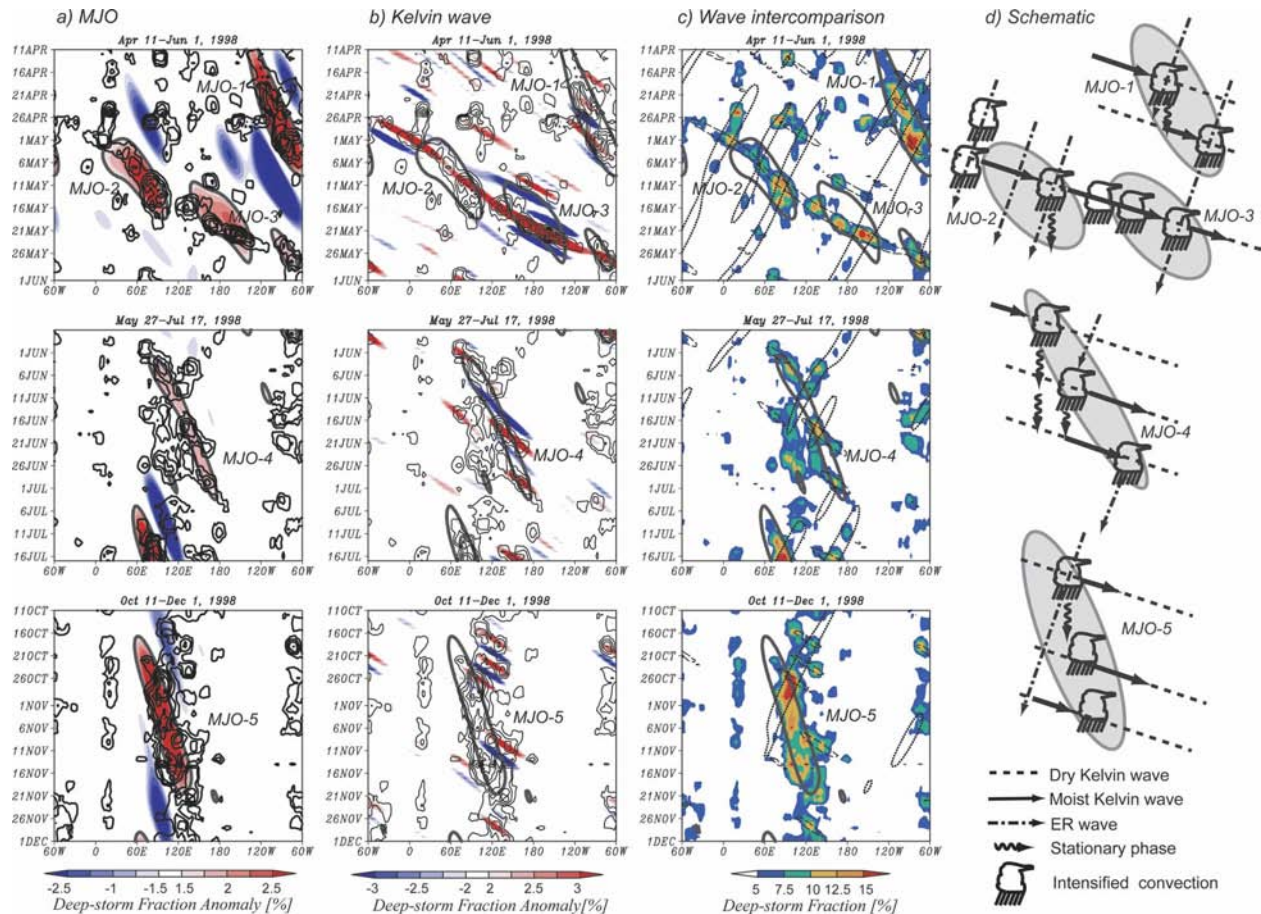
FIG. 2.1. Time–longitude diagram of deep-storm fraction for different time periods. (a) The MJO-filtered anomaly (color) and unfiltered field contoured at an interval of 2.5% starting with 5%. (b) The Kelvin-filtered anomaly (color) as well as the unfiltered field. The MJO-filtered anomaly at the +1.5% level is superimposed for reference. (c) The unfiltered field in colors superimposed with the anomalies of the filtered Kelvin wave (at +2% in dashed contour) and ER wave (at +1% in dotted contour). (d) A schematic representation of wave interactions and a resultant stationary convective phase. The dry Kelvin wave is simply extrapolated from the moist counterpart in the schematic, where difference in propagation speed between the dry and moist waves is ignored for brevity.

may be explained by a near-zero group velocity of the ER wave as indicated by Wheeler et al. (2000).

c. Internal structure of the waves

Figure 4 shows daily infrared images with 850-hPa horizontal wind anomaly and the 3-hourly time–longitudinal section averaged over 10°S–10°N. In the time–longitude diagram, the westward migration of cloud systems constitutes a fine structure embedded in eastward propagating mesoscale convective systems (MCS) as originally discovered by Nakazawa (1988). Westward-moving cloud systems are also evident in the envelope of the stationary convective phase that belongs to MJO-9, staying active to the west of 100°E until 5 May. This stationary convective phase is associated with strong westerly wind anomaly after 28 April as seen in the daily images. The westerly anomaly gains

a southward component and eventually turns into an easterly anomaly as it goes on through the Southern Hemisphere.

An MCS originating from the Maritime Continent moves to the east together with the Kelvin wave and eventually reaches beyond the date line on 4 May. This MCS is primarily centered between 5°N and the equator throughout the propagation, where the intertropical convergence zone (ITCZ) is located during this period. A notable exception is that the MCS expands northward up to 10°N in a cyclonic motion from 29 to 30 April, when the ER wave intersects the Kelvin wave as indicated in the time–longitude diagram. The MCS then breaks up into a pair moving in opposite directions: an MCS continuously brought to the east by the Kelvin wave and another to the west by the ER wave. The wind anomaly associated with the Kelvin and ER
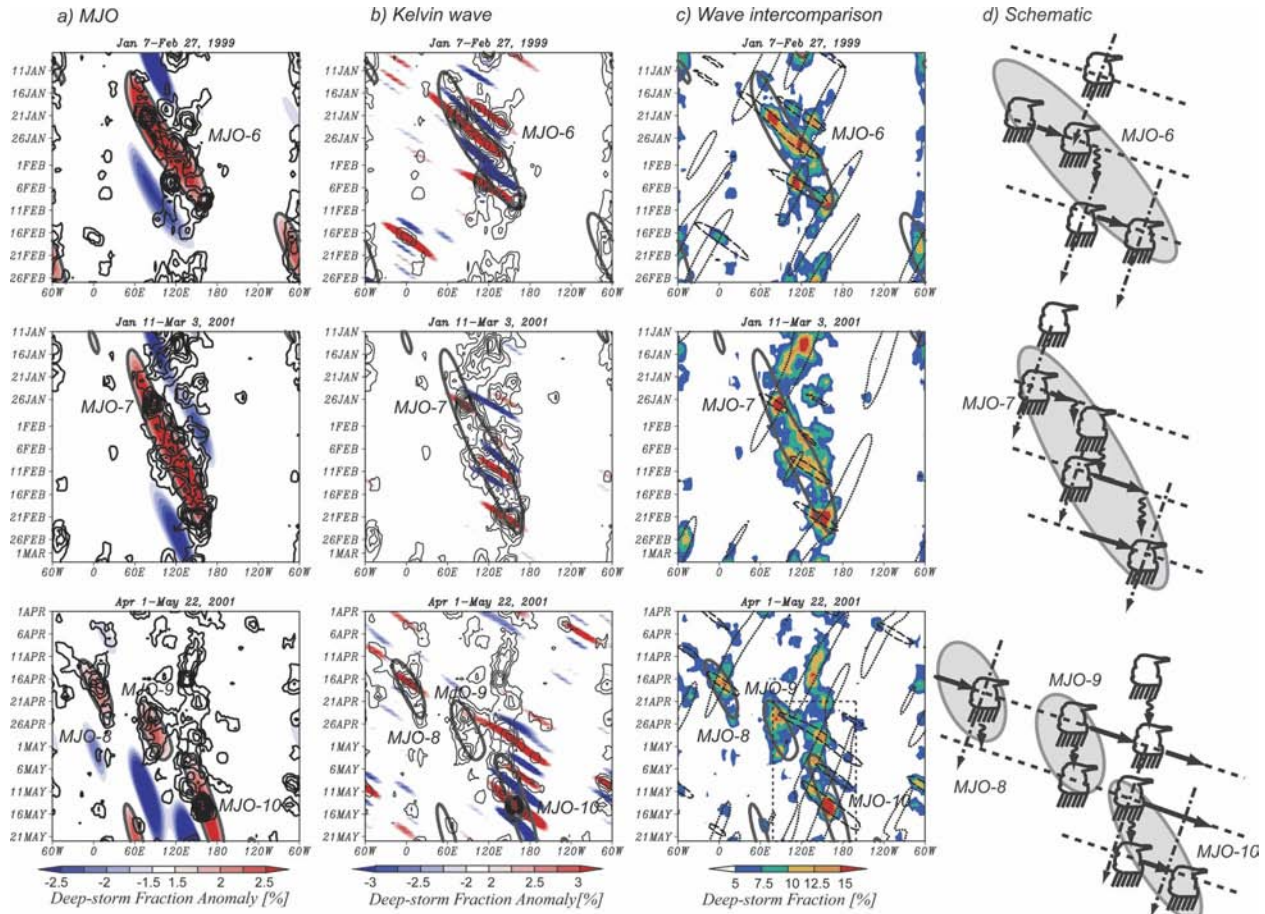
FIG. 2.2. Same as Fig. 2.1, except for the different dates shown. The dashed box in the lower panel of (c) indicates the spatial and temporal coverage used for GMS analysis (Figs. 4 and 5).

waves generally shows patterns typical to each mode. In 3 May, for instance, a gyre is readily identified for an MCS accompanied with the ER wave at 5°N and 135°E, while another MCS linked with the Kelvin wave

(2.5°N and 170°W) is associated with zonally dominant wind anomaly as expected.

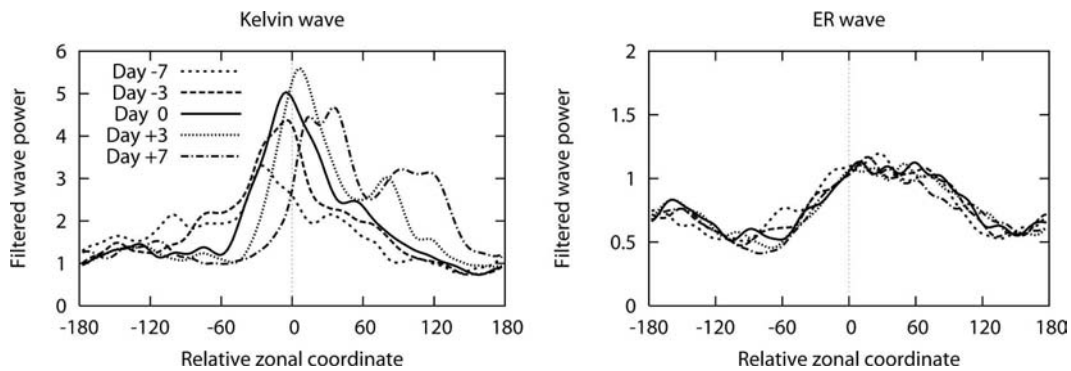The subsequent evolution is shown in Fig. 5. The MCS that arrived from the east at the Maritime Con-

FIG. 3. Lag composite for (left) the Kelvin-wave power and (right) ER wave power with respect to the MJO peak, defined by local maxima in the filtered MJO field of the deep-storm fraction. The ordinate shows the square of deep-storm fraction anomaly [in (%)^2] filtered by each wave. The abscissa represents zonal coordinate [in (°)] relative to the MJO maximum.
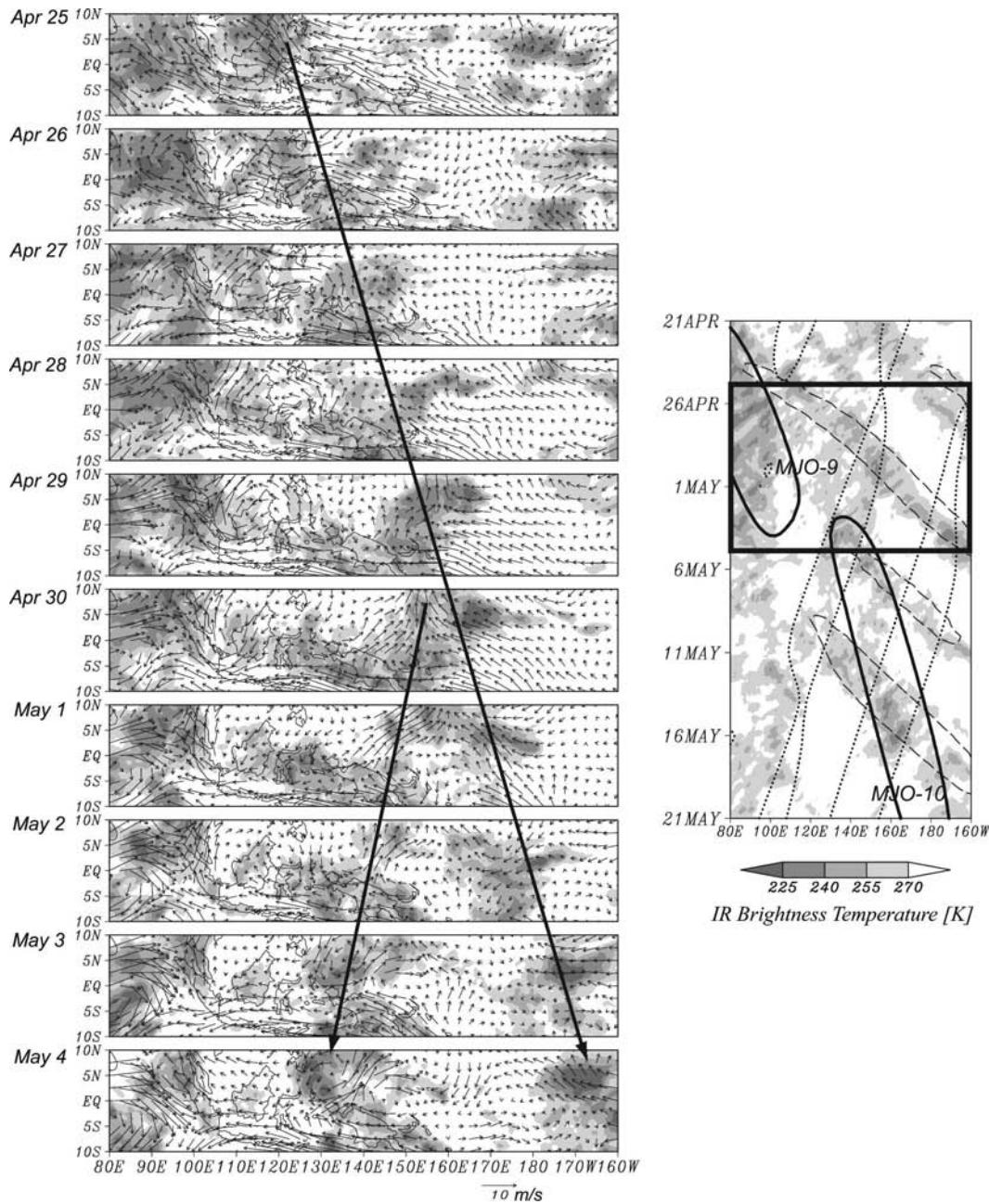
FIG. 4. Daily-averaged GMS infrared images on a half-degree grid superposed (left) by 850-hPa horizontal wind anomaly on a 2.5-degree grid and (right) by 3-hourly time–longitude diagram for the 10S°–10°N latitudinal band from 21 April to 20 May 2001. Contour lines are taken from Fig. 2c. The time period covered by the left panels is indicated by thick-framed box. Arrows indicate the movement of mesoscale convective systems (see text).

tinent on 4 May (Fig. 4) is split again on 5 May. A new MCS is born and heads east in response to the Kelvin wave. The old MCS continues moving slowly to the west and spawns another MCS heading east on 9 May, when the ER wave meets the next ridge of the Kelvin wave. The newest MCS quickly grows in size immediately after it merges with another system approaching

from the east on 10 May. This westward-moving MCS, designated by dashed arrow, does not belong to the ER wave, because it is located in a trough of the filtered ER wave and concentrated within $\pm 5°$ in latitude dissimilarly to the ER wave. This system is more likely associated with a tropical depression (TD)-type disturbance (Takayabu and Nitta 1993). The merged MCS keeps
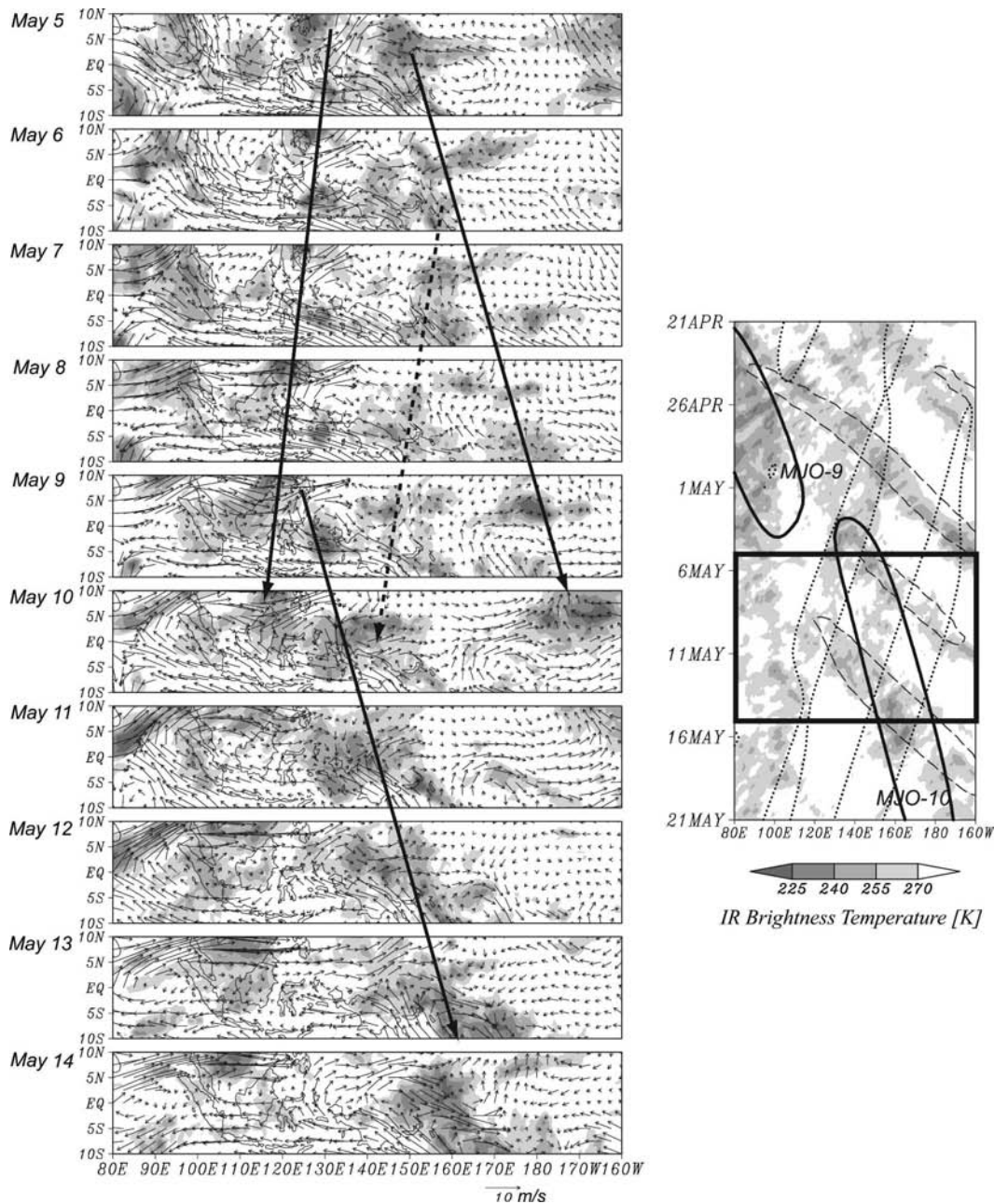
FIG. 5. Same as Fig. 4 but daily images for a subsequent time period.

heading east and develops to a very intense system in the west Pacific by 14 May. It can be seen in the time–longitude diagram that this intensified MCS is located where the Kelvin wave meets an incoming ER wave. Interestingly, although the ER wave involved here is not clearly visible in the infrared images, it is traceable in wind anomaly as a gyre moving to the west in the Southern Hemisphere from 180° on 9 May to 160°E on 13 May. The final stage of the MCS on 14 May turns out to be part of MJO-10 together with another MCS that

builds up over the Maritime Continent earlier on 3 and 4 May.

5. Discussion

a. Interrelationship among different waves

The case studies and a brief composite analysis demonstrated in the previous section motivate us to give some thought to the possible relationship between the Kelvin and ER waves and the MJO. A number of pre-

vious studies have pointed out the critical roles of both the Kelvin and ER waves in association with the MJO. Hayashi and Sumi (1986) discovered in their aqua-planet simulations that the eastward convectively coupled wave with a period of 30 days is disintegrated into the Kelvin and Rossby waves as soon as the moist processes are turned off. A model study by Lau et al. (1989) demonstrated that the Kelvin and Rossby waves take part in the dynamical adjustment to reconcile an imbalance between large-scale circulation and heating fields. Observational studies also found evidence for a coupled Rossby–Kelvin wave in composite analyses of the MJO (Nakazawa 1988; Hendon and Salby 1994; Salby and Hendon 1994; Takayabu et al. 1999).

Some preceding studies have also focused on the interactions between different modes of the tropical oscillations. Dunkerton and Crum (1995) analyzed a 10-yr record of OLR measurement to find some evidence for low-frequency ($\sim$30–60 days) oscillations interacting with high-frequency ($\sim$2–15 days) eastward propagation. Considering that their high-frequency propagation is likely the Kelvin wave, their findings support our composite analysis (Fig. 3) showing a strong Kelvin wave peak collocated with the MJO maximum. Straub and Kiladis (2003) discovered that the MRG and TD-type activity is enhanced with the MJO convective envelope, and that the Kelvin wave is more active in the east of the MJO than within the MJO envelope. While the notable Kelvin wave activity in the east of the MJO is also seen in Fig. 3 of this paper, the present result shows a high concentration of the Kelvin wave within the MJO envelope in contrast to Straub and Kiladis (2003). The disagreement is perhaps because Straub and Kiladis (2003) focused their analysis on boreal summers, when the MJO is not active in general (Madden 1986; Roundy and Frank 2004a). Preliminary results from an OLR-based long-term analysis underway indicate the significant seasonal variation that the Kelvin wave is in the east of the MJO for boreal summer, while the Kelvin wave is clearly located within the MJO envelope during austral summer (not shown). Figure 3 exhibits both these aspects because it is based on all seasons together. Roundy and Frank (2004b,c) demonstrated that interactions between the eastward- and westward-propagating intraseasonal oscillations (roughly corresponding to the MJO and ER wave, respectively, by the current definition) modulate the amplitudes of these waves. These existing studies all seem to imply that interactions between different tropical waves are commonly observed and can play some role in MJO propagation. In this study, it is found in Fig. 2 that distinct spots of enhanced convection are often collocated with areas where a ridge of the Kelvin wave

intersects with an intruding ER wave. The convective amplification may be induced by the Kelvin and ER waves interacting with each other in a way similar to that discussed by Dunkerton and Crum (1995) and Roundy and Frank (2004b,c).

It is beyond the scope of this paper to extensively explore the physical basis behind the present results. We, nevertheless, forward a hypothesis concerning MJO propagation, where a group of consecutive ridges of the convectively coupled Kelvin wave are presumed to be a seed of the MJO formation. The ignition and maintenance of convective activity associated with the MJO are in part brought by the interaction of the Kelvin wave with the ER wave. Convection occasionally remains intensive beyond the control of the large-scale waves, which forms a stationary convective phase. It is speculated that stationary convective phase is maintained by a convective system driven by self-generated diabatic circulation that has grown strong enough to overwhelm the wave-induced circulation. An entire system including intensified convection and stationary convective phase(s) slowly moves to the east, because the Kelvin wave dominates the ER wave in both speed and amplitude. The predominance of the Kelvin wave over the ER wave in association with MJO is implied by Fig. 3. This whole propagation system is unlikely ascribable to a linear superposition of the Kelvin and ER waves because of the nonlinearity involved in the moist processes as well as the presence of the stationary convective phase. The resultant unique mode orthogonal to both the Kelvin and ER waves is presumably responsible for the distinct MJO peak found in the space–time spectrum.

This idea, if true, raises some important questions. What modulates neighboring Kelvin waves so that they are grouped around the MJO? What determines the efficiency with which the wave interaction controls convective intensity, if the ER wave is ubiquitous both inside and outside the MJO envelope as observed in Fig. 2? Physical factors beyond wave dynamics perhaps need to be considered to address these questions. The development of deep convection is, for example, closely related to local geophysical conditions such as SST. Masunaga et al. (2005) suggested the existence of a regime-independent threshold of 28°–29°C above which SST favors deep storm systems in the tropical Pacific. Lower-tropospheric moisture and radiative processes are also potential key parameters characterizing environmental states that affect convective activity.

The linear theory of the Kelvin and ER waves, moreover, involves no intrinsic mechanism to preferentially select a particular intraseasonal time scale. A typical MJO period of 40–50 days is too slow to be attributed

to any linear waves in the Tropics. On the other hand, this time scale allows a cyclic change in environmental conditions between those favorable and unfavorable to the development of active convection (Bladé and Hartmann 1993; Hu and Randall 1994; Flatau et al. 1997; Sobel and Gildor 2003). This locally regulated thermodynamic system associated with the MJO manifests itself in observed geophysical parameters such as SST, wind speed, surface heat flux, humidity, precipitation, OLR, and solar insolation (Lin and Johnson 1996; Zhang 1996; Kemball-Cook and Weare 2001; Stephens et al. 2004). Section 5b reexamines the connection between the observed MJO time scale and background geophysical parameters derived from satellite measurements.

b. Variability in environmental conditions

Geophysical parameters examined here include SST, low (liquid) clouds, columnar water vapor (CWV), near-surface wind speed, latent heating, net atmospheric radiative heating by clouds, and cloud short-wave forcing at the surface. These variables are derived primarily from TRMM measurements from the methodology described by L'Ecuyer and Stephens (2003). In brief summary, the algorithm first retrieves ice clouds, liquid clouds, and precipitation from TRMM infrared and microwave radiometric measurements. Background atmosphere and surface parameters are obtained from the data archives provided by European Centre for Medium-Range Weather Forecasts (EC-MWF) as well as the TRMM Microwave Imager (TMI)-based datasets produced by Remote Sensing Systems (RSS). Broadband shortwave and longwave fluxes are then synthesized by forward radiative transfer calculations. A complete description of the algorithm with error analysis can be found in L'Ecuyer and Stephens (2003). The area fractions of shallow and deep precipitation systems are determined using the Masunaga et al. (2005) categorization based on VIRS IR T_b and PR echo-top height: shallow rain is identified by VIRS IR T_b warmer than 260 K and PR echo-top height lower than 4 km, while the deep category is as defined earlier in section 2.

For the cross-correlation analysis performed below, all variables are averaged over oceanic scenes across the whole globe between 10°S and 10°N at the zonal and temporal resolutions of 1° and 1 day, respectively. The cross-correlation function between each variable and the MJO-filtered deep-storm fraction is computed. Time series at different longitudes are considered independent samples. The 2-yr period from January 1998 to December 1999 is analyzed, but the first and last 60
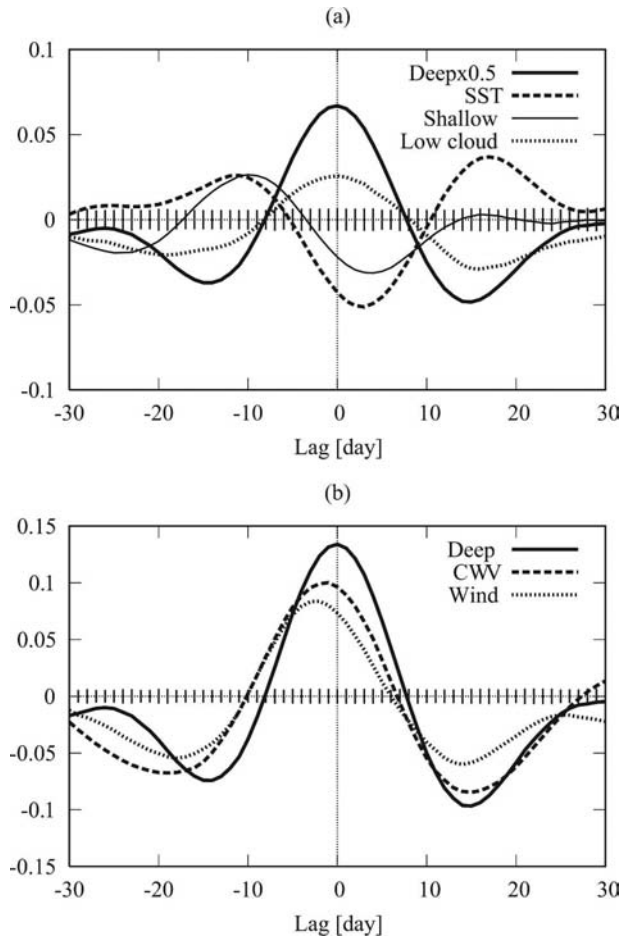

FIG. 6. Cross-correlation function of the MJO-filtered deep-storm fraction with (a) (unfiltered) deep-storm fraction (rescaled by a factor of 0.5), SST, shallow-cumulus fraction, and low-cloud fraction, and with (b) deep-storm fraction, CWV, and near-surface wind speed. A negative lag means that the MJO-filtered deep-storm fraction lags. Vertical bars at the abscissa indicate the significance level at 95%.

days are removed from the filtered deep-storm fraction due to the data loss by the windowing (see section 4a).

The cross-correlation functions are shown in Fig. 6. Correlation is statistically significant beyond the 95% level outside the range indicated by vertical bars. Deep storm systems have a nearly symmetric cross-correlation function with a pronounced maximum at lag 0, reflecting the MJO cycle itself. The cross correlation of SST indicates that sea surface exhibits a gradual warming trend in advance of the MJO maximum (at lag 0) by more than 10 days. Low clouds are negatively correlated during the SST warming period. During the same period, shallow convection gradually increases peaking 10 days prior to the MJO maximum. The lack of an accompanying increase during this period in low cloudiness suggests an increasingly efficient conversion

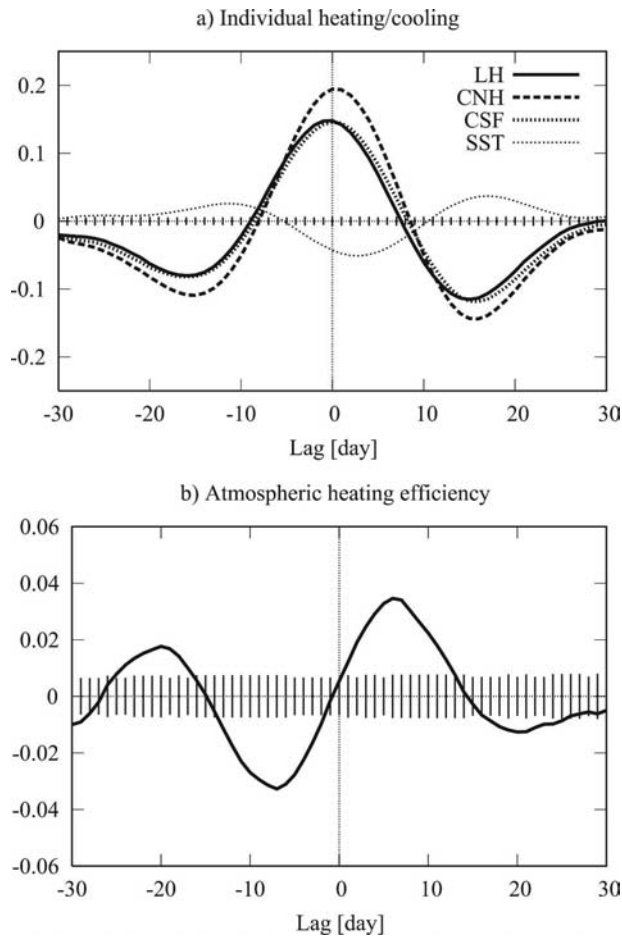a) Individual heating/cooling

b) Atmospheric heating efficiency

FIG. 7. Same as Fig. 6 but for (a) latent heating (LH), net atmospheric radiative heating by clouds (CNH), cloud shortwave forcing (CSW) at the surface, and SST, and for (b) atmospheric heating efficiency r_H.

from cloud liquid water to precipitation. The resultant lower-tropospheric moistening is observed in the cross correlation of CWV (Fig. 6b). The fact that near-surface wind increases in phase with CWV implies that wind-induced evaporation is important as well for moistening the lower troposphere. Both the wind speed and CWV lead deep storm systems by a few days. SST starts to decrease as deep convection intensifies. A warm ocean surface begins to recover about 10 days after the MJO maximum as the sky clears, the air dries, and the wind calms.

In Fig. 7a the latent heating, net atmospheric heating by clouds (hereafter the cloud heating), and cloud shortwave forcing at the surface are plotted as cross-correlation functions. The cross correlation of SST is duplicated from Fig. 6 for reference. The latent heating and cloud heating closely reflect the development and dissipation of convective activity associated with the

MJO. The cloud shortwave forcing at the surface is also in phase.

A closer examination reveals that the cloud heating and latent heating are not precisely symmetric about lag 0. The latent heating slightly (by a day) leads the cloud heating, and the influence of the cloud heating remains longer after the MJO maximum than that of the latent heating. This reflects the fact that the cloud heating is enhanced as high clouds detrained from precipitation cores develop behind the convectively matured stage. The role of cloud heating relative to latent heating is most clearly evident in terms of the atmospheric heating efficiency, r_H, defined as the ratio of cloud heating to latent heating (L'Ecuyer et al. 2005). While r_H has a close connection to the conventional precipitation efficiency defined as the ratio of precipitation to total condensate, r_H is a more direct representative of the local gradient of atmospheric heating, which ultimately leads to changes in the tropospheric stability associated with precipitating cloud systems. Although the phase difference between latent heating and cloud heating is as small as a day or two, their ratio or r_H could have a critical impact on an intraseasonal time scale typical of the MJO. It can be demonstrated by a simple mathematical model as follows. Consider two sinusoidal functions with a phase lag $\delta\theta$ with a constant offset a. For $|\delta\theta| \ll 1$,

$$\frac{a + \cos(\theta + \delta\theta)}{a + \cos\theta} \approx 1 - \delta\theta \frac{\sin\theta}{a + \cos\theta}.$$

The resultant function oscillates at the period of 2π independently of $\delta\theta$. The smaller $\delta\theta$ is, the smaller the amplitude is while it does not affect the period at all. As such, the leading oscillation dominates the other in the ratio, whatever small the lead is, throughout the first half of the cycle and the relation is turned over during the rest of the period.

This conceptually explains a fundamental trend in the correlation of r_H with the MJO cycle as shown in Fig. 7b, which shows that r_H is anticorrelated with the MJO-filtered deep-storm fraction for 15 days preceding the MJO maximum, while the correlation is positive for the following 15 days. The antisymmetric pattern in r_H suggests the contrasting roles of cloud heating between the destabilization that primes the atmosphere for convection prior to the maximum convective activity and the subsequent stabilizing influence of the cloud long-wave heating of the upper troposphere.

Figures 6 and 7 support the MJO-related cycle swinging between stable and unstable atmospheric environments as suggested by previous work. An increase of SST in advance of the MJO maximum was found in the

literature (e.g., Nakazawa 1995; Zhang 1996; Hendon and Glick 1997). The anticorrelation of low clouds with SST is indicative of strong insolation under suppressed boundary layer clouds as discussed by Flatau et al. (1997), Hendon and Glick (1997), and Stephens et al. (2004). The moistening of the free troposphere in response to increasing shallow convection is pointed out by Kemball-Cook and Weare (2001). The rapid increase of wind speed and water vapor ahead of the MJO maximum supports the result of Zhang (1996) that the surface latent-heat flux slightly leads the most active convection. It is noted, however, that the phase lag is not distinct enough to let an evaporation–wind feedback mechanism (Emanuel 1987; Neelin et al. 1987) alone drive the MJO. The decrease of SST with intensifying convection is presumably due to the combined effects of the oceanic vertical mixing, wind-induced evaporative cooling, and reduced insolation by cloud shielding (Flatau et al. 1997). The close correlation between the latent heating and radiative heating is consistent with the findings by Lin and Mapes (2004). The whole picture suggested by the present result closely resembles the humidistat theory proposed by Stephens et al. (2004).

In section 5a we discussed the possibility that a sequence of consecutive Kelvin waves could be a key to account for MJO propagation. The above radiative–hydrological cycle may serve as a modulator that controls the amplitude of convectively coupled waves quasi-periodically on an intraseasonal time scale. This is possibly a mechanism by which neighboring Kelvin wave ridges are grouped together. Furthermore, low-level convergence brought by the Kelvin wave, especially when it coincides with that due to the ER wave, could intensify convection more efficiently if it takes place in a more unstable phase of the atmospheric cycle. This may also be a part of the cycle of convective variation associated with the MJO. The combination of locally induced oscillation and wave-driven propagation as a forced response is essentially an observational realization of the discharge–recharge theory of Bladé and Hartmann (1993) aside from differences in details. The observed thermodynamic structure of the MJO was found to be supportive of the discharge–recharge hypothesis also in the analysis performed by Benedict and Randall (2006, manuscript submitted to *J. Atmos. Sci.*).

c. Implications for model studies

These results emphasize the fact that for model simulations to reproduce the MJO it is critical that they account for all factors controlling convective activity with proper flexibility. The convective response to low-level convergence can be either reinforced or weakened depending on the environmental conditions involving SST, moisture, surface wind, solar insolation, and long-wave atmospheric cooling. Without the modulation by these conditions, the MJO would be resolved into linear waves propagating independently (e.g., Hayashi and Sumi 1986). Slingo et al. (1996) concluded that AGCMs generally have difficulty in simulating intraseasonal oscillations with periods slower than 30 days. This may indicate that while climate models have achieved overall success in reproducing the moist Kelvin wave (which has a period of 30 days for $h = 24$ m at $k = 1$), the modulation of convective activity by changes in the background state is not appropriately modeled. More recent work indicates that the nature of simulated eastward propagation is significantly affected by introducing a wind–SST interaction (Flatau et al. 1997), a cloud–radiation interaction (Lee et al. 2001; Raymond 2001), or their combination (Sobel and Gildor 2003).

As an alternative to conventional cloud-parameterization schemes, multiscale modeling framework (MMF) or superparameterization (Grabowski 2001; Randall et al. 2003) allows a flexible treatment of the convective response to the environmental conditions. Grabowski (2003), investigating an MJO-like structure simulated in a superparameterized aquaplanet model, discovered that its development exhibited a strong sensitivity to the free-tropospheric moisture. This confirms the importance of the moistening by shallow convection (section 5b) that preconditions the development of the MJO. Further progress in the model capability of realizing the MJO will be critical since only a limited number of variables can be extracted directly from observations. Applying a frequency–wavenumber analysis and a filtering technique to simulated outputs would help diagnose the model performance in comparison with observations.

6. Summary

The present paper examines observed properties of the MJO by analyzing TRMM PR and VIRS measurements acquired from December 1997 to December 1999 and from December 2000 to June 2001. A frequency–wavenumber analysis of these datasets reveals general spectral features relevant to convectively coupled equatorial waves that are consistent with previous work. The PR swath is so narrow that TRMM sampling errors tend to degrade the statistical significance of spectral signals for high-frequency modes relative to the NOAA OLR product, while lower-frequency modes are still prominent in the TRMM

spectrum. Deep-storm fraction estimated by PR and VIRS in the frequency–wavenumber domain shows the predominance of wavenumbers 5–8 for the moist Kelvin wave. Another outstanding spectral feature appears at a period of about 40 days and wavenumbers 1–7, recognized as the spectral representation of the MJO. A weaker spectral signal corresponding to the $n = 1$ ER wave is also identified.

A filtering analysis of 10 MJO events in time–longitude space suggests that a group of consecutive Kelvin waves are often collocated with an MJO envelope. These Kelvin waves encompass distinct regions of enhanced convection at the intersection with an intruding ER wave, launching a stationary convective phase, or an intensive convective event left behind outgoing waves, in some cases. A lag composite diagram indicates that the Kelvin wave, approaching the MJO from the west before the MJO grows most active, is strongest when it spatially and temporally coincides with the MJO peak. The Kelvin wave emanating in the east of the MJO is observed once the peak phase of MJO activity passed. The composite ER wave exhibits much weaker correlation with the MJO peak with no temporal variation to its east. A case study based on GMS imagery and 850-hPa winds confirms a coherent trend in the behavior of MCSs.

Cross-correlation analysis of observed geophysical parameters yields a result consistent with existing scenarios on the intraseasonal cycle regulating atmospheric stability. Sea surface exhibits a warming trend for 10 days or more prior to the MJO maximum, while low clouds are anticorrelated with the MJO-filtered deep-storm fraction during this period. Following an increase of shallow convection, CWV increases and near-surface winds intensify, leading deep convection by a few days. All the parameters return to their initial state when about 30 days passed after the MJO maximum. The net atmospheric heating by clouds and cloud shortwave forcing at the surface exhibit nearly coherent correlation with latent heating. A slight phase lag, however, between cloud atmospheric heating and latent heating results in a cross-correlation function antisymmetric about lag 0 for the atmospheric heating efficiency r_H, suggesting a dramatic shift in the role of cloud radiative heating before and after the peak in deep convective activity.

As the time period analyzed in the present paper is limited, further investigations based on a longer-term data analysis are required to ensure statistical robustness. It is, moreover, beyond the scope of the present paper and possible the observations employed to determine a specific mechanism that provides a comprehensive explanation for the above findings. Future model

studies with improved capability of resolving the moist-convective processes at the root of the MJO are therefore crucial. A hypothetical explanation, nevertheless, emerges from the current results that the MJO may be understood in terms of a series of active convection associated with a group of the Kelvin wave. The interaction of the Kelvin wave with the ER wave might assist the triggering and maintenance of convective activity within the MJO envelope. These linear waves coupled with convection as well as the occasional onset of the stationary convective phase behave as if they together constitute a slow propagation system, which appears to be loosely modulated by a locally regulated radiative-hydrological cycle. We speculate that this system is responsible for the distinct spectral mode corresponding to the MJO.

REFERENCES

Bladé, I., and D. L. Hartmann, 1993: Tropical intraseasonal oscillations in a simple nonlinear model. *J. Atmos. Sci.,* **50,** 2922–2939.

Cho, H.-K., K. P. Bowman, and G. R. North, 2004: Equatorial waves including the Madden–Julian oscillation in TRMM rainfall and OLR data. *J. Climate,* **17,** 4387–4406.

Dunkerton, T. J., and F. X. Crum, 1995: Eastward propagating ~2- to 15-day equatorial convection and its relation to the tropical intraseasonal oscillation. *J. Geophys. Res.,* **100,** 25 781–25 790.

Emanuel, K. A., 1987: An air–sea interaction model of intraseasonal oscillations in the Tropics. *J. Atmos. Sci.,* **44,** 2324–2340.

——, J. D. Neelin, and C. S. Bretherton, 1994: On large-scale circulations in convecting atmospheres. *Quart. J. Roy. Meteor. Soc.,* **120,** 1111–1143.

Flatau, M., P. J. Flatau, P. Phoebus, and P. P. Niiler, 1997: The feedback between equatorial convection and local radiative and evaporative processes: The implications for intraseasonal oscillations. *J. Atmos. Sci.,* **54,** 2373–2386.

Grabowski, W. W., 2001: Coupling cloud processes with the large-

scale dynamics using the cloud-resolving convection parameterization (CRCP). *J. Atmos. Sci.,* **58,** 978–997.

——, 2003: MJO-like coherent structures: Sensitivity simulations using the cloud-resolving convection parameterization (CRCP). *J. Atmos. Sci.,* **60,** 847–864.

Gruber, A., 1974: The wavenumber-frequency spectra of satellite-measured brightness in the Tropics. *J. Atmos. Sci.,* **31,** 1675–1680.

——, and A. F. Krueger, 1984: The status of the NOAA outgoing longwave radiation data set. *Bull. Amer. Meteor. Soc.,* **65,** 958–962.

Hayashi, Y., and D. G. Golder, 1993: Tropical 40–50- and 25–30-day oscillations appearing in realistic and idealized GFDL climate models and the ECMWF dataset. *J. Atmos. Sci.,* **50,** 464–494.

Hayashi, Y.-Y., and A. Sumi, 1986: The 30–40-day oscillations simulated in an "aqua planet" model. *J. Meteor. Soc. Japan,* **64,** 451–466.

Hendon, H. H., and M. L. Salby, 1994: The life cycle of the Madden–Julian oscillation. *J. Atmos. Sci.,* **51,** 2225–2237.

——, and J. Glick, 1997: Intraseasonal air–sea interaction in the tropical Indian and Pacific Oceans. *J. Climate,* **10,** 647–661.

Hu, Q., and D. A. Randall, 1994: Low-frequency oscillations in radiative–convective systems. *J. Atmos. Sci.,* **51,** 1089–1099.

Kemball-Cook, S. R., and B. C. Weare, 2001: The onset of convection in the Madden–Julian oscillation. *J. Climate,* **14,** 780–793.

Lau, K.-M., L. Peng, C. H. Sui, and T. Nakazawa, 1989: Dynamics of super cloud clusters, westerly wind bursts, 30-60 day oscillations and ENSO: An unified view. *J. Meteor. Soc. Japan,* **67,** 205–219.

L'Ecuyer, T. S., and G. L. Stephens, 2003: The tropical oceanic energy budget from the TRMM perspective. Part I: Algorithm and uncertainties. *J. Climate,* **16,** 1967–1985.

——, H. Masunaga, and C. D. Kummerow, 2005: Variability in the characteristics of precipitation systems over the tropical Pacific. Part II: Implications for atmospheric heating. *J. Climate,* **19,** 1388–1406.

Lee, M.-L., I.-S. Kang, J.-K. Kim, and B. E. Mapes, 2001: Influence of cloud-radiation interaction on simulating tropical intraseasonal oscillation with an atmospheric general circulation model. *J. Geophys. Res.,* **106,** 14 219–14 233.

Lin, J.-L., and B. E. Mapes, 2004: Radiation budget of the tropical intraseasonal oscillation. *J. Atmos. Sci.,* **61,** 2050–2062.

Lin, X., and R. H. Johnson, 1996: Kinematic and thermodynamic characteristics of the flow over the western Pacific warm pool during TOGA COARE. *J. Atmos. Sci.,* **53,** 695–715.

Lindzen, R. D., 1967: Planetary waves on beta-planes. *Mon. Wea. Rev.,* **95,** 441–451.

Madden, R. A., 1986: Seasonal variations of the 40–50-day oscillation in the Tropics. *J. Atmos. Sci.,* **43,** 3138–3158.

——, and P. R. Julian, 1971: Detection of a 40–50-day oscillation in the zonal wind in the tropical Pacific. *J. Atmos. Sci.,* **28,** 702–708.

——, and ——, 1972: Description of global-state circulation cells in the tropics with a 40–50-day period. *J. Atmos. Sci.,* **29,** 1109–1123.

——, and ——, 1994: Observation of the 40–50-day tropical oscillation—A review. *Mon. Wea. Rev.,* **122,** 814–837.

Masunaga, H., T. S. L'Ecuyer, and C. D. Kummerow, 2005: Variability in the characteristics of precipitation systems over the tropical Pacific. Part I: Spatial structure. *J. Climate,* **18,** 823–840.

Matsuno, T., 1966: Quasi-geostrophic motions in the equatorial area. *J. Meteor. Soc. Japan,* **44,** 25–43.

Nakazawa, T., 1986: Mean features of 30–60-day variations as inferred from 8-year OLR data. *J. Meteor. Soc. Japan,* **64,** 777–786.

——, 1988: Tropical super clusters within intraseasonal variations over the west Pacific. *J. Meteor. Soc. Japan,* **66,** 823–839.

——, 1995: Intraseasonal oscillations during the TOGA-COARE IOP. *J. Meteor. Soc. Japan,* **73,** 305–319.

Neelin, J. D., I. M. Held, and K. H. Cook, 1987: Evaporation–wind feedback and low-frequency variability in the tropical atmosphere. *J. Atmos. Sci.,* **44,** 2341–2348.

Randall, D., M. Khairoutdinov, A. Arakawa, and W. Grabowski, 2003: Breaking the cloud parameterization deadlock. *Bull. Amer. Meteor. Soc.,* **84,** 1547–1564.

Raymond, D. J., 2001: A new model of the Madden–Julian oscillation. *J. Atmos. Sci.,* **58,** 2807–2819.

Reed, R. J., and E. E. Recker, 1971: Structure and properties of synoptic-scale wave disturbances in the equatorial western Pacific. *J. Atmos. Sci.,* **28,** 1117–1133.

Roundy, P. E., and W. M. Frank, 2004a: A climatology of waves in the equatorial region. *J. Atmos. Sci.,* **61,** 2105–2132.

——, and ——, 2004b: Effects of low-frequency wave interactions on intraseasonal oscillations. *J. Atmos. Sci.,* **61,** 3025–3040.

——, and ——, 2004c: Applications of a multiple linear regression model to the analysis of relationships between eastward- and westward-moving intraseasonal modes. *J. Atmos. Sci.,* **61,** 3041–3048.

Salby, M. L., and H. H. Hendon, 1994: Intraseasonal behavior of clouds, temperature, and motion in the Tropics. *J. Atmos. Sci.,* **51,** 2207–2224.

Slingo, J. M., and Coauthors, 1996: Intraseasonal oscillations in 15 atmospheric general circulation models: Results from an AMIP diagnostic subproject. *Climate Dyn.,* **12,** 325–357.

Sobel, A. H., and H. Gildor, 2003: A simple time-dependent model of SST hot spots. *J. Climate,* **16,** 3978–3992.

Stephens, G. L., P. J. Webster, R. H. Johnson, R. Engelen, and T. S. L'Ecuyer, 2004: Observational evidence for the mutual regulation of the tropical hydrological cycle and tropical sea surface temperatures. *J. Climate,* **17,** 2213–2224.

Straub, K. H., and G. N. Kiladis, 2003: Interactions between the boreal summer intraseasonal oscillations and higher-frequency tropical wave activity. *Mon. Wea. Rev.,* **131,** 945–960.

Takayabu, Y. N., 1994: Large-scale cloud disturbances associated with equatorial waves. Part I: Spectral features of the cloud disturbances. *J. Meteor. Soc. Japan,* **72,** 433–448.

——, and M. Murakami, 1991: The structure of super cloud clusters observed in 1–20 June 1986 and their relationship to easterly waves. *J. Meteor. Soc. Japan,* **63,** 105–125.

——, and Ts. Nitta, 1993: 3–5 day-period disturbances coupled with convection over the tropical Pacific Ocean. *J. Meteor. Soc. Japan,* **71,** 221–246.

——, T. Iguchi, M. Kachi, A. Shibata, and H. Kanzawa, 1999: Abrupt termination of the 1997–98 El Niño in response to a Madden-Julian oscillation. *Nature,* **402,** 279–282.

von Storch, H., and F. W. Zwiers, 1999: *Statistical Analysis in Climate Research.* Cambridge University Press, 484 pp.

Wheeler, M., and G. N. Kiladis, 1999: Convectively coupled equatorial waves: Analysis of clouds and temperature in the wavenumber–frequency domain. *J. Atmos. Sci.,* **56,** 374–399.

——, and K. M. Weickmann, 2001: Real-time monitoring and prediction of modes of coherent synoptic to intraseasonal tropical variability. *Mon. Wea. Rev.,* **129,** 2677–2694.

——, and H. H. Hendon, 2004: An all-season real-time multivariate MJO index: Development of an index for monitoring and prediction. *Mon. Wea. Rev.,* **132,** 1917–1932.

——, G. N. Kiladis, and P. J. Webster, 2000: Large-scale dynamical fields associated with convectively coupled equatorial waves. *J. Atmos. Sci.,* **57,** 613–640.

Yanai, M., and M. Murakami, 1970: Spectrum analysis of symmetric and antisymmetric equatorial waves. *J. Meteor. Soc. Japan,* **48,** 331–347.

——, B. Chen, and W.-W. Tung, 2000: The Madden–Julian oscillation observed during the TOGA COARE IOP: Global view. *J. Atmos. Sci.,* **57,** 2374–2396.

Zangvil, A., 1975: Temporal and spatial behavior of large-scale disturbances in tropical cloudiness deduced from satellite brightness data. *Mon. Wea. Rev.,* **103,** 904–920.

Zhang, C., 1996: Atmospheric intraseasonal variability at the surface in the tropical western Pacific Ocean. *J. Atmos. Sci.,* **53,** 739–758.